Materials Advances

ROYAL SOCIETY OF CHEMISTRY

PAPER

View Article Online
View Journal | View Issue

Cite this: *Mater. Adv.*, 2022, 3, 5087

BA_2XBr_4 (X = Pb, Cu, Sn): from lead to lead-free halide perovskite scintillators†

Lina Jaya Diguna, *[a] Luke Jonathan,[a] Muhammad Haris Mahyuddin,[b] Arramel,[cd] Francesco Maddalena,[e] Irma Mulyani,[f] Djulia Onggo,[f] Abdellah Bachiri,[g] Marcin Eugeniusz Witkowski,[g] Michal Makowski,[g] Dominik Kowal,[h] Winicjusz Drozdowski *[g] and Muhammad Danang Birowosuto *[h]

Received 4th March 2022,
Accepted 16th May 2022

DOI: 10.1039/d2ma00258b

rsc.li/materials-advances

Solution-processed hybrid organic–inorganic lead halide perovskites have potential for next generation X-ray imaging applications. Here, we discuss the effect of Pb replacement by Cu or Sn on the optical and scintillation properties of the high-light-yield and fast crystal scintillators of BA_2PbBr_4. By replacing Pb with Cu or Sn, the measured bandgap shifts from 3.59 to 3.90 and 3.44 eV, while the photoluminescence decay time slows down from 3.0 ns to 1.3 and 8.5 μs, respectively. The bandgaps and the structures are also validated by density functional theory calculations. Although BA_2CuBr_4 and BA_2SnBr_4 have large Stokes shifts of 2.06 and 1.13 eV, respectively, both crystals show no radioluminescence (RL) at room temperature (RT). Temperature-dependent RL measurements demonstrate that BA_2PbBr_4 has negative thermal quenching, while Pb replacement by Cu or Sn results in strong thermal quenching, affecting the light yields at RT. Despite slow decay times and low light yields for BA_2CuBr_4 and BA_2SnBr_4, this study opens new understanding for lead-free perovskite crystals and the trends in their scintillation properties.

Introduction

Lead halide perovskites have attracted great interest as scintillating materials.[1–4] Due to their large effective atomic mass and mass density, all-inorganic perovskites are favored for the application of stopping high-energy radiation. Nevertheless, the radiation absorption lengths for their quantum dots[2,5] and nanosheets[6] are much smaller than those in bulk due to the presence of the ligands and/or adhesives, which make the packing fractions much lower than those in bulk. The small Stokes shift also creates some issues with reabsorption.[7] On the other hand, hybrid organic–inorganic perovskite (HOIP) lead halide crystals have been considered for the application of low-energy radiation scintillators, *e.g.* X-ray, though recently they were also reported to be effective for gamma-ray and neutron spectroscopy with good energy resolution.[8,9] For these two-dimensional (2D) HOIP lead halide crystals, the bromide crystals are more stable and have larger light yields than iodide ones.[8] Butylammonium lead bromide (BA_2PbBr_4) scintillators are already known to have high light yields between 8000 and 40 000 photons per MeV and fast decay time between 5 and 8 ns at various excitation energies and crystal qualities.[8,10,11] However, these materials pose an environmental issue due to the presence of lead cations in their structure that cause severe health hazards. Moreover, replacing the lead cation with other divalent cations may increase the Stokes shift of the materials.[7] An approach to replace lead with other metal cations has been attempted such as with manganese (Mn),[12] copper (Cu),[13] tin (Sn),[14] and antimony (Sb).[15]

[a] *Department of Renewable Energy Engineering, Universitas Prasetiya Mulya, Kavling Edutown I.1, Jl. BSD Raya Utama, BSD City, Tangerang 15339, Indonesia. E-mail: lina.diguna@prasetiyamulya.ac.id*
[b] *Research Group of Advanced Functional Materials and Research Center for Nanoscience and Nanotechnology, Institut Teknologi Bandung, Jl. Ganesha 10, Bandung 40132, Indonesia*
[c] *Department of Physics, National University of Singapore, 2 Science Drive 3, Singapore 117551, Singapore*
[d] *Nano Center Indonesia, Jl. PUSPIPTEK, South Tangerang, Banten 15314, Indonesia*
[e] *CINTRA UMI CNRS/NTU/THALES 3288, Research Techno Plaza, 50 Nanyang Drive, Border X Block, Level 6, Singapore 637553, Singapore*
[f] *Inorganic and Physical Chemistry Research Group, Faculty of Mathematics and Natural Sciences, Institut Teknologi Bandung, Jl. Ganesha 10, Bandung 40132, Indonesia*
[g] *Institute of Physics, Faculty of Physics, Astronomy, and Informatics, Nicolaus Copernicus University in Torun, ul. Grudziadzka 5, Torun 87-100, Poland. E-mail: wind@fizyka.umk.pl*
[h] *Łukasiewicz Research Network-PORT Polish Center for Technology Development, Stabłowicka 147, 54-066 Wrocław, Poland. E-mail: muhammad.birowosuto@port.lukasiewicz.gov.pl*

† Electronic supplementary information (ESI) available. See https://doi.org/10.1039/d2ma00258b

In this work, we aim to explore the effect of Pb substitution by Cu or Sn on the optical and scintillation properties of solution-processed 2D BA_2PbBr_4 perovskite. First, we confirmed the crystal structure with X-ray diffraction (XRD) characterizations and then performed photoluminescence (PL) measurements to demonstrate the emission from these perovskite crystals at room temperature (RT). Optical absorption characterization shows the bandgap red-shift for lead-free crystals compared to the BA_2PbBr_4 crystal, in which the similar bandgap values for all these crystals may relate to the same maximum theoretical light yields. We observe large Stokes shifts for lead-free perovskite crystals compared to the BA_2PbBr_4 crystal. Those large Stokes shifts may be beneficial to enhance the light yields by reducing self absorption.[4,7] Temperature-dependent radioluminescence (RL) spectra of perovskite crystals provide detailed information on light yields between 350 and 10 K. As previously reported, BA_2PbBr_4 shows negative thermal quenching behavior,[8] *i.e.* stronger PL is observed with increasing temperature, which could be practically beneficial in reducing cooling needs for the scintillator and improving performance at higher temperatures. In fact, Pb substitution by Cu or Sn in the crystals leads to the presence of strong thermal quenching. Although these lead-free crystals demonstrate RL at low temperature, the light yield is reduced at higher temperature, in particular for the BA_2CuBr_4 crystal. For thermoluminescence (TL), only BA_2SnBr_4 exhibits strong depth traps while the others are trap free. Although the thermal quenching affects the scintillation properties for lead-free perovskite crystals at high temperature, this study will provide insight into designing and developing new lead-free perovskite scintillators.

Experimental methods

Perovskite crystal preparation

Butylammonium bromide (BABr, 98%), lead bromide ($PbBr_2$, 98%), hydrobromic acid (HBr, 48%), tin(II) bromide ($SnBr_2$), butylamine (BA, 99.5%), and dimethyl sulfoxide (DMSO, anhydrous) were purchased from Sigma-Aldrich. Copper(II) oxide (CuO, ACS reagent) was purchased from Fisher Scientific. All chemicals were used without further purification.

BA_2PbBr_4 crystals were synthesized from solution, with a previously used method.[9,11] The precursors $PbBr_2$ and BABr were dissolved in DMSO in stoichiometric amounts up to a concentration of 3 M. The solution was stirred at 100 °C for 2 hours under N_2 in order to fully dissolve the precursors and then cooled down to room temperature. The solution was left to evaporate slowly for a period ranging from two weeks to 1 month until large crystals formed. The crystals were filtered out of the solution, then washed several times with diethyl ether, finally dried and stored in vacuum until characterization.

The method to synthesize BA_2CuBr_4 and BA_2SnBr_4 was adopted from published literature.[16] To prepare BA_2CuBr_4, CuO (0.48 g, 6 mmol) was dissolved in warm HBr (5 mL) under constant stirring. To this solution, a solution of excess BA (5 mL, 50 mmol) in 5 mL HBr was added and then a saturated mixture was obtained. Finally, methanol (50 mL) was added to the saturated solution mixture and this solution was warmed for 30 minutes with continued stirring. After the solution mixture was allowed to reach room temperature, the dark violet product of BA_2CuBr_4 was crystallized. For the preparation of BA_2SnBr_4, a solution of $SnBr_2$ (0.28 g, 1 mmol) was dissolved in warm HBr (5 mL) under constant stirring in an argon atmosphere. To this solution, an aqueous solution of BABr (0.61 g, 4 mmol) in 1 mL H_2O was added and stirring of the solution mixture was continued for 30 minutes. After the solution was allowed to cool to room temperature, it was stored in a freezer for 5 days, during this process, the yellow product of BA_2SnBr_4 was crystallized. This product was recrystallized by dissolving the initial crude product of BA_2SnBr_4 in a small amount of ethanol and subsequently keeping the saturated solution at room temperature for 1–2 days until large-size crystals were formed in a glass beaker.

X-ray diffraction

Powder X-ray diffraction (XRD) data were recorded on a Bruker D8 Advance AXS diffractometer with graphite-monochromatized Cu Kα radiation (λ = 1.54059 Å). The data acquisition was undertaken at RT under Bragg–Brentano geometry with the speed of scanning as 5 s per step and a step size of 0.01. XRD diffractograms were then analyzed using FullProf software.[17]

X-ray photoelectron spectroscopy

X-ray photoelectron spectroscopy (XPS) experiments were carried out using an X-ray source of magnesium Kα with a typical excitation energy output of 1254 eV. The impinged spot size on the sample is about 1 mm in diameter. All the reported XPS spectra were calibrated by reference to the Ag $3d_{5/2}$ peak position (centered at 368.10 eV) of a silver polycrystalline foil cleaned *via* standard argon ion sputtering treatment.

PL, time-resolved PL, absorption, and PL quantum yields

PL measurements were performed at room temperature (RT) using free-space excitation and collection through a visible-near-infrared microscope objective (Nikon 20×, Nikon Corporation, Tokyo, Japan, NA = 0.40). The sample was excited *via* a 30 kHz picosecond pulsed diode laser (Master Oscillator Fibre Amplifier, Picoquant, Picoquant GmbH, Berlin, Germany, excitation wavelength at 266 or 355 nm, pulse width 50 ps, and power of 10 μW). The PL measurement was based on the epifluorescence method. PL spectra were recorded using an AvaSpec-HERO spectrometer (Avantes BV, Apeldoorn, The Netherlands). For time-resolved photoluminescence measurements (TRPL), a pico-second pulsed diode laser with repetition rates between 30 kHz and 10 MHz (Master Oscillator Fiber Amplifier, Picoquant, excitation wavelength at 266 or 355 nm, pulse width 50 ps) was employed. The emission was then selected by a band filter at 425 and 532 ± 25 nm and detected by a single-photon avalanche photodiode (APD) connected to a time-correlated single-photon counting acquisition module (Edinburgh Instruments, TCC900, Edinburgh Instruments Ltd, Livingstone, United Kingdom). In PL and TRPL measurements,

the excitation wavelength of 266 nm was used for BA_2CuBr_4, while that of 355 nm was used for BA_2PbBr_4 and BA_2SnBr_4. Absorption spectra of perovskite crystals were obtained using an ultraviolet–visible (UV-vis) spectrometer (Shimadzu, Model UV-2450). PL quantum yields (PLQY) were measured with the Labsphere integrating sphere explained in our previous works.[14,18] To check the validity of our PLQY measurements, we used Nanolumi $CsPbBr_3$ quantum dots as references as they had already been measured previously by the company.[14,18] All optical measurements were performed after a pre-heating step so that there was no afterglow or traps in the samples.

RL, TL, and glow curves

For all these measurements, we used one integrated setup. It consists of an Inel XRG3500 X-ray generator Cu-anode tube, 45 kV/10 mA, an Acton Research Corporation SpectraPro-500i monochromator, a Hamamatsu R928 photomultiplier tube (PMT), and an APD Cryogenic Inc. closed-cycle helium cooler. First, we recorded low temperature afterglow at 10 K by exposing the crystals to X-rays for 10 minutes. Then, we measured TL glow curves at temperatures between 10 and 350 K with a heating rate of about 0.14 K s^{-1}. Afterwards, we measured the RL at different temperatures between 350 and 10 K starting from the highest to lowest temperatures in order to avoid possible contributions to the emission yield from the thermal release of charge carriers.

Density functional theory calculations

The Kohn–Sham formulation[19,20] as implemented in the Vienna *Ab initio* Simulation Package (VASP)[21,22] was used for the density functional theory (DFT) calculations. The Projector Augmented Wave (PAW) method[23,24] was used to describe the interaction between ion cores and electrons. The electron exchange–correlation was treated by the generalized gradient approximation (GGA) based on the Perdew–Burke–Ernzerhof (PBE) functional.[25] The rotationally invariant GGA+U approach introduced by Dudarev *et al.*[26] was used with the effective Hubbard parameter U_{eff} being 4.0, 4.0, and 5.0 eV, respectively, for the Cu d,[27] Pb p, and Sn p orbitals. Spin-polarized calculations were performed only for the BA_2CuBr_4. The plane wave basis sets with a cut-off energy of 500 eV were used for all calculations. The Brillouin zone with a k-point grid of $5 \times 5 \times 1$ according to the Monkhorst–Pack scheme[28] was used. The zero-damping D3 method[29] was adopted to account for the dispersion correction. During calculations, all atoms were allowed to fully relax. The conjugate gradient method was employed for cell optimizations, and the calculations were considered to converge when the maximum forces on each atom were less than 0.01 eV $Å^{-1}$.

Results and discussion

Fig. 1 shows the appearances and structures of the BA_2XBr_4 crystals. The appearances of three representative single crystals of BA_2PbBr_4, BA_2CuBr_4, and BA_2SnBr_4 under ultraviolet excitation are shown in Fig. 1(a), (b) and (c), respectively. BA_2PbBr_4 has blue emission as reported earlier.[8] By replacing Pb with Sn, the crystal emission shifts from blue to green, though the crystal thickness is still very thin due to the preferred lateral orientation growth in the two-dimensional perovskite. In contrast, BA_2CuBr_4 has dim emission and its thicker crystal compared to those with Pb and Sn indicates less preferred lateral orientation growth. XRD diffractograms of BA_2PbBr_4, BA_2CuBr_4, and BA_2SnBr_4 are shown in Fig. 1(d), (e), and (f), respectively, with the inset corresponding to each crystal structure. Rietveld refinement for these crystals was performed using FullProf software and the results are shown in Fig. S1 (ESI†). The orthorhombic phase can be found with *Pbca* space group and the refined lattice parameters of BA_2PbBr_4 (a = 8.3369 Å, b = 8.2259 Å, c = 27.6238 Å), BA_2CuBr_4 (a = 8.2498 Å, b = 7.8098 Å, c = 25.8735 Å) and BA_2SnBr_4 (a = 8.1340 Å, b = 8.0268 Å, c = 26.9590 Å). The observed mismatches in peak intensities are due to considerable texture in the samples obtained from finely ground crystals for the XRD measurements. For BA_2CuBr_4, the comparison with $CuBr_2$ in monoclinic phase confirms the negligible amount of $CuBr_2$ as shown in Fig. S1(d) (ESI†).[30] The observed prominent peaks located in the lower angle represent the (001)-orientated layer structures, where two inorganic sheets are separated by a layer of organic molecules as shown in the insets.[8] The same organic cation used in these crystals is responsible for the similar position of these prominent peaks. We then calculate density of states (DOS) using DFT and the optical bandgap (E_g). The band structure, total (black) and projected (color) DOS of BA_2PbBr_4, BA_2CuBr_4, and BA_2SnBr_4 crystals are shown in Fig. 1(g), (h), and (i), respectively. The blue line represents Pb p, Cu d, and Sn p in each crystal, while the pink and red lines represent BA p, and Br p orbitals, respectively. We obtain calculated bandgaps (E_g^{cal}) of 3.36, 3.84, and 2.68 eV for BA_2PbBr_4, BA_2CuBr_4, and BA_2SnBr_4, respectively, the former of which agrees well with the previous theoretical study using the hybrid HSE06 functional (3.37 eV).[31] These similar E_g values result in the similar estimated maximum light yields for all these crystals. The band structure of BA_2CuBr_4 in Fig. 1(h), in particular, shows a state near the Fermi energy (E_F). This strongly indicates that BA_2CuBr_4 is a p-type semiconductor. In addition, the band structure of the spin-down BA_2CuBr_4 in Fig. S2(b) (ESI†) shows an in-band state, which is characteristic of Cu^{2+}.

Fig. 2(a–c) present the chemical state elucidations of the respective perovskite samples measured by the XPS technique. The prominent broad peaks of Pb 4f core levels in BA_2PbBr_4 at 143.11 and 138.26 eV respectively correspond to the $4f_{5/2}$ and $4f_{7/2}$, indicating the expected signature of lead-based perovskite that typically can be found in the literature.[9,32–34] In regard to the spectral line shape of the Cu 2p core levels presented in Fig. 2(b), we found that the peak separation between two prominent signals gives a peak difference close to ~19.8 eV, reflecting the spin–orbit coupling of Cu 2p states that is commonly found in the perovskite system.[13,35] The main peaks of Cu $2p_{1/2}$ (951.5 eV) and Cu $2p_{3/2}$ (931.6 eV) are found for the BA_2CuBr_4 sample. We note that the third sample contains an Sn-constituent based on the Sn 3d core level shown in Fig. 2(c). Two broad peaks corresponding to $3d_{3/2}$ and $3d_{5/2}$ signals were

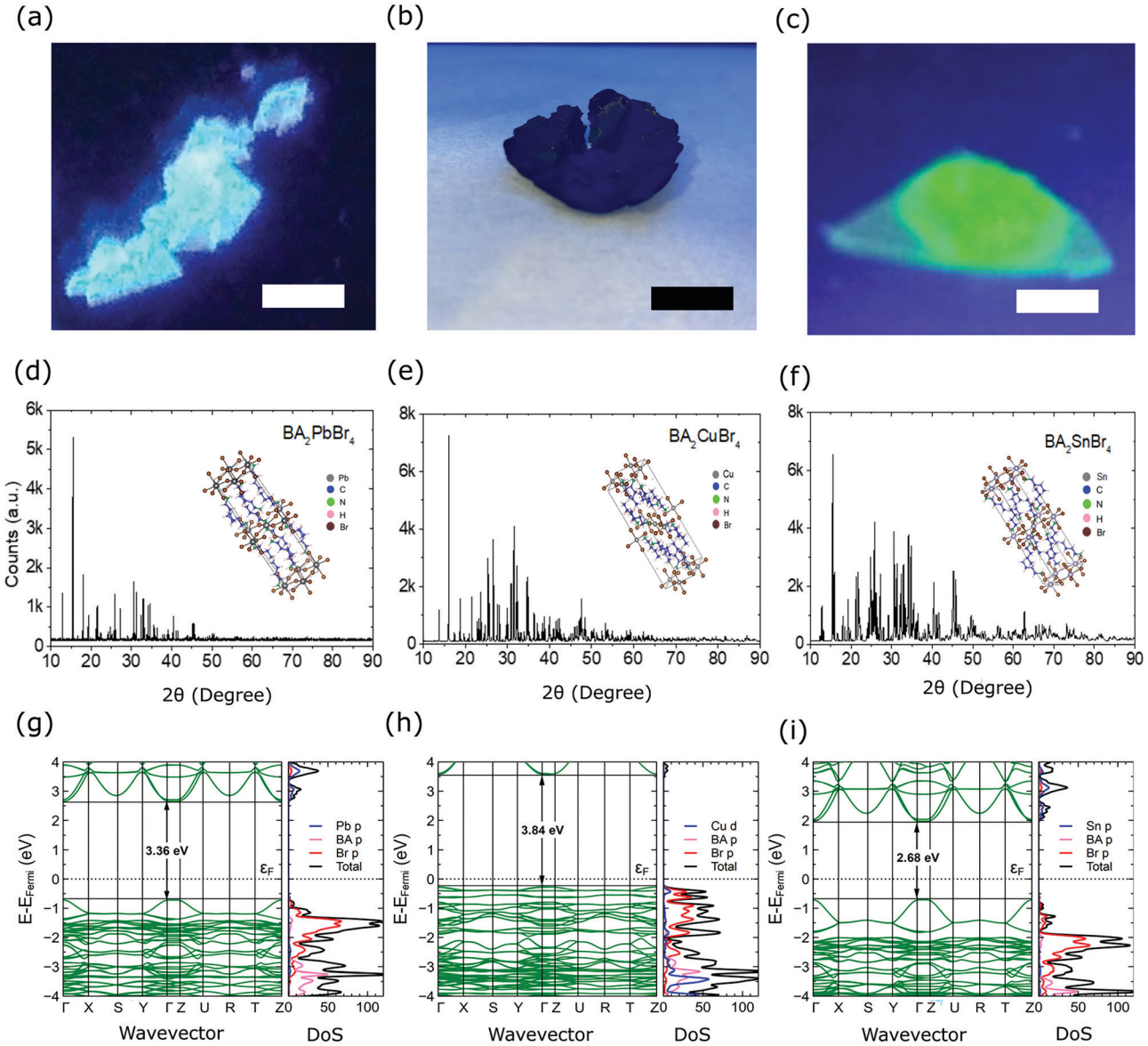

Fig. 1 Appearance and structure of BA_2XBr_4 (X = Pb, Cu, Sn). Photographs of (a) BA_2PbBr_4, (b) BA_2CuBr_4, and (c) BA_2SnBr_4 crystals under commercial ultraviolet lamp excitation. Scale bar is 5 mm. XRD diffractograms of (d) BA_2PbBr_4, (e) BA_2CuBr_4, and (f) BA_2SnBr_4 crystals with their crystal structures (insets). The band structure, total (black) and projected (color) DOS of (g) BA_2PbBr_4, (h) BA_2CuBr_4, and (i) BA_2SnBr_4 crystals. Blue line represents Pb p, Cu d, and Sn p in (g), (h), and (i), while pink and red lines represent BA p, and Br p orbitals, respectively.

observed at 494.97 and 486.57 eV, respectively. This result is in agreement with the previous Sn-hybrid perovskite crystals.[14,36] The other contributions such as core levels (C 1s, N 1s and Br 3d) to confirm the chemical integrity of the hybrid perovskite crystals are summarized in Fig. S3 (ESI†).

In all crystals, the ratio of these core levels is found to be similar due to the use of the same organic cation (BA) and halide anion (Br). Absorption and PL spectra of the crystals are shown in Fig. 2(d–f). BA_2PbBr_4 crystal has an absorption peak at 346 nm, while those with Cu and Sn are located at 245 and 355 nm, respectively. From the absorption spectra, the experimental bandgap (E_g^{exp}) could be obtained as 3.59, 3.90 and 3.44 eV for BA_2PbBr_4, BA_2CuBr_4, and BA_2SnBr_4, respectively, which are comparable to the above E_g^{cal} values, see Fig. S4 (ESI†). The E_g^{exp} of BA_2PbBr_4 is also consistent with the previous report.[10] BA_2PbBr_4 shows a PL peak at 437 nm (2.84 eV) with an extra small peak at the shorter wavelength (414 nm (3.00 eV)). The presence of double-peaked PL is in accordance with our previous study of BA_2PbBr_4.[11] For the class of 2D lead halide perovskite materials, double-peaked emission has been reported as an indication of the presence of a dual bandgap resulting from the different bulk and surface states.[8,37,38] Those effects were also probed in the same class of materials by TRPL[39] and cathodoluminescence.[40] The low intensity at 414 nm demonstrates Stokes-shift-induced self absorption by the metal coordination sphere deformation in 2D hybrid lead bromide.[41] The cause of this effect is also strengthened by the previous observation of the large 414 nm-PL intensity in thin

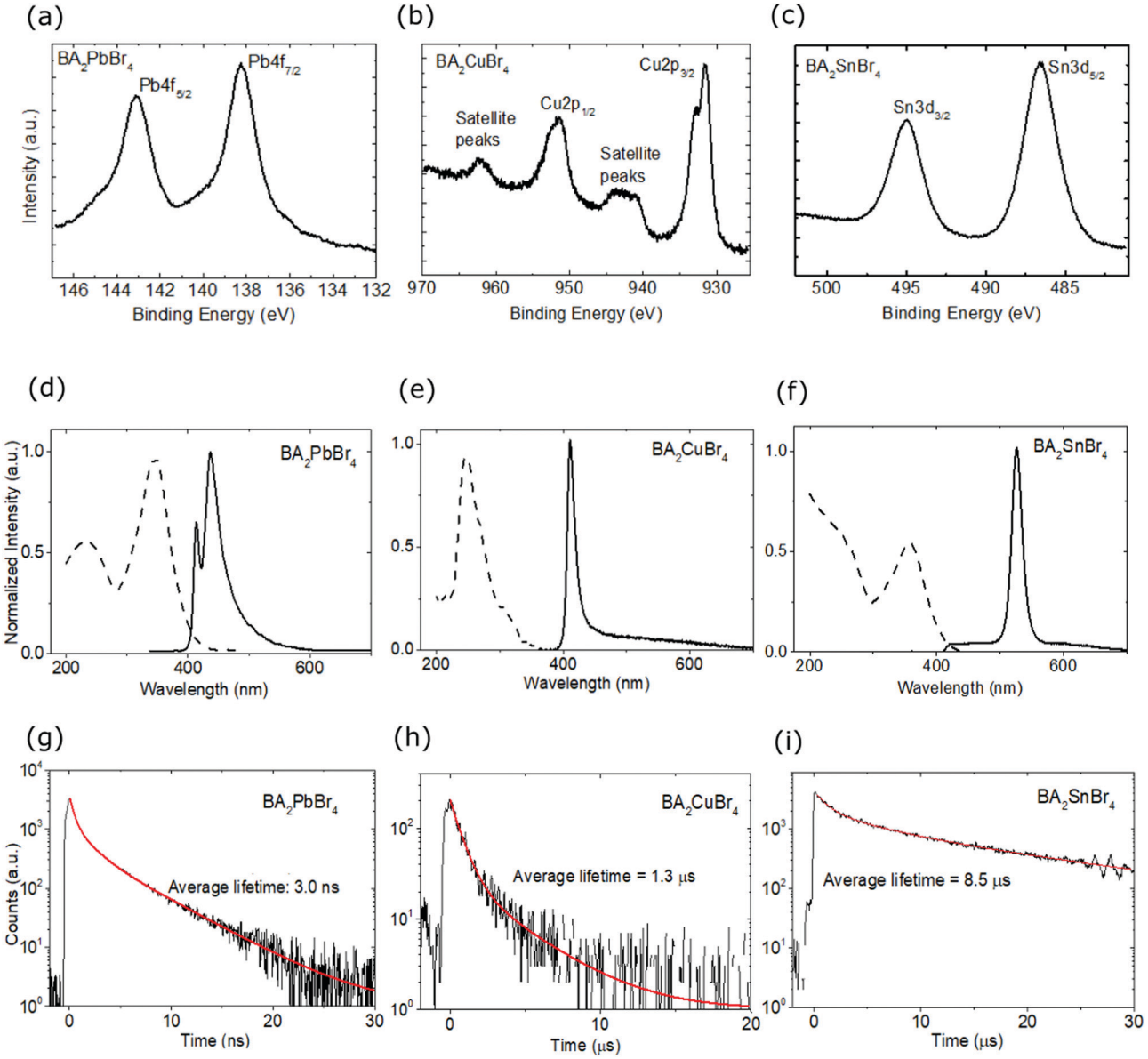

Fig. 2 Surface characteristics and optical properties of BA_2XBr_4 (X = Pb, Cu, Sn). XPS signals from (a) Pb 4f, (b) Cu 2p, and (c) Sn 3d levels and their corresponding binding energy in BA_2PbBr_4, BA_2CuBr_4, and BA_2SnBr_4 crystals, respectively. Absorption and PL spectra of (d) BA_2PbBr_4, (e) BA_2CuBr_4, and (f) BA_2SnBr_4 crystals, recorded at room temperature (RT) shown in dashed and solid lines, respectively. TRPL decay curves of (g) BA_2PbBr_4, (h) BA_2CuBr_4, and (i) BA_2SnBr_4 crystals, monitored at 425 nm emission for BA_2PbBr_4 and BA_2CuBr_4 crystals, and at 532 nm emission for the BA_2SnBr_4 crystal.

film and the disappearance of the same peak in RL spectra.[11] Replacement of Pb with Cu or Sn shifts the PL peak at 414 nm to a shorter wavelength at 411 nm (3.02 eV) and longer wavelength at 526 nm (2.36 eV), respectively. In those materials, the short wavelength peaks have maximum intensity showing less self absorption. From those values, the Stokes shifts for BA_2PbBr_4, BA_2CuBr_4, and BA_2SnBr_4 are 0.59, 2.06, and 1.13 eV, respectively. We expect that those large Stokes shifts will help to prevent the self absorption in the scintillators.[4,7] Narrower PL spectra are also observed for the lead-free crystals. Here, the full width at half maximum (FWHM) values of BA_2CuBr_4 and BA_2SnBr_4 are 19 and 24 nm, respectively, while those for PEA_2CuBr_4 and PEA_2SnBr_4 are about 100 nm.[13,42] The use of a short organic cation has been reported to have a lesser contribution to the charge dynamics due to weaker electron–phonon interaction.[13] To examine the PL decay characteristics, the emission at 425 nm was monitored for BA_2PbBr_4 and BA_2CuBr_4, and the emission at 532 nm was monitored for BA_2SnBr_4. As shown in Fig. 2(g), BA_2PbBr_4 crystal has a fast average decay time of 3.0 ns. This observation is in good agreement with the previous reports.[8,10] Substituting Pb with Cu or Sn causes a slower PL decay with average decay times of 1.3 and 8.5 μs as shown in Fig. 2(h) and (i), respectively.

Fig. 3(a) represents the RL spectra of the crystals at 10 and 300 K, taken after being sure that there are no afterglow and trapped charge carriers existing in the crystals. BA_2PbBr_4 shows RL for measurements at both 10 and 300 K, while BA_2CuBr_4, and BA_2SnBr_4 crystals only show RL at 10 K. At 10 K, BA_2PbBr_4

and BA_2CuBr_4 crystals have similar RL peak positions at 421 nm (2.95 eV) and 420 nm (2.95 eV), and narrow RL spectra with FWHM of 6 nm (0.04 eV) and 7 nm (0.03 eV), respectively. BA_2SnBr_4 crystal at 10 K shows a RL peak at a longer wavelength of 539 nm (2.30 eV) with a FWHM of 7 nm (0.05 eV), and with increasing the temperature to 300 K, the RL peak of BA_2PbBr_4 crystal demonstrates a red-shift to 435 nm (2.85 eV) with a broader FWHM of 24 nm (0.16 eV). Fig. 3(b–d) show afterglow and TL curves of BA_2PbBr_4, BA_2CuBr_4, and BA_2SnBr_4, respectively. BA_2PbBr_4 and BA_2CuBr_4 crystals show very short afterglow and no traps are observed. The absence of traps is related to the very short chain of the organic cation in comparison with other 2D HOIP crystals.[12] On the other hand, BA_2SnBr_4 crystal shows slower decay afterglow as shown in Fig. 3(d) with the TL curve satisfactorily fitted by the two exponential decay function. The TL decay components for BA_2SnBr_4 crystal are 53.2 s (12%) and 516.8 s (88%). Pb substitution with Sn seems to contribute to this slower decay, indicating the presence of traps. To evaluate trap concentrations and depths, temperature-dependent TL was recorded with a heating rate of 0.14 K s^{-1}. It can be clearly seen that only BA_2SnBr_4 crystal shows a TL glow-curve, meaning the presence of traps compared to BA_2PbBr_4 and BA_2CuBr_4 crystals. As shown in Fig. S5 (ESI†), two traps are observed in BA_2SnBr_4 crystal. These two traps do not have much difference in their depth energies, *i.e.* 452 and 622 meV, even though the total number of traps for the energy of 622 meV is three-fold compared to that of 452 meV.

Temperature-dependent RL spectra mapping at different temperatures from 10 K to 350 K is depicted in Fig. 4(a–c) for BA_2PbBr_4, BA_2CuBr_4, and BA_2SnBr_4, respectively. BA_2PbBr_4 has higher RL intensity at higher temperature. On the other hand, BA_2CuBr_4 and BA_2SnBr_4 exhibit high RL intensities for the measurement at 10 K and these signals strongly reduce at room temperature. The characteristics of negative thermal quenching are then studied by fitting the temperature-dependent integrated RL intensities as shown in Fig. 4(d) with the model proposed by Shibata.[43] The fitting parameters are shown in Table S1 (ESI†). All samples exhibit negative thermal quenching behaviour. BA_2PbBr_4 shows relatively small activation energies and large coefficients for both positive and negative thermal quenching.[11] This means that the light yield is relatively stable for the entire temperature range. In comparison with BA_2PbBr_4, BA_2CuBr_4 has the strongest thermal and less negative thermal quenching, whereas both activation energies and coefficients are small. BA_2SnBr_4 shows large activation energies and small coefficients in both negative thermal and thermal quenching resulting in significant effects in negative thermal and thermal quenching.

Since the light yield of X-ray scintillation conversion is inversely proportional to the E_g^{exp},[4,44] BA_2PbBr_4, BA_2CuBr_4, and BA_2SnBr_4 crystals are theoretically expected to have maximum light yields up to 122 000, 94 000 and 126 000 photons per MeV, respectively, only if both PL quantum yields (PLQYs) and transfer efficiencies are unity. From the integrated PL intensity measured with integrating sphere, see Fig. S6 (ESI†), PLQYs for all crystals can be estimated. Since we have thick single crystals, we slightly modified the calculations for obtaining the values in Table S2 (ESI†) from those in de Mello *et al.*[45]

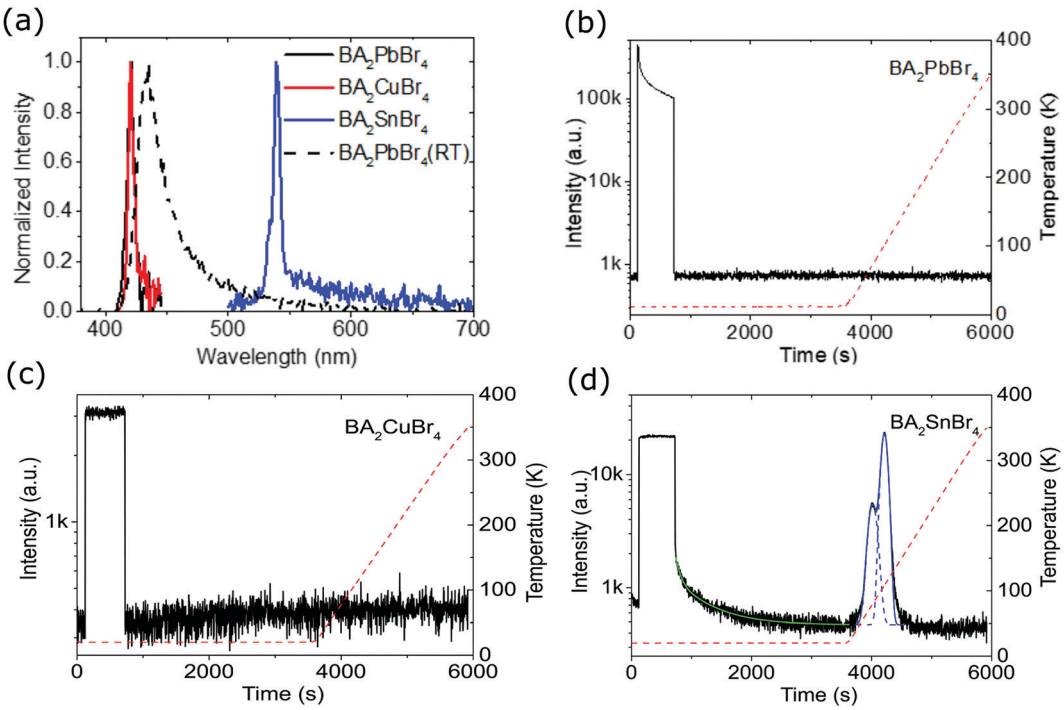

Fig. 3 (a) RL spectra of BA_2PbBr_4, BA_2CuBr_4, and BA_2SnBr_4 crystals at 10 K and 300 K. Steady-state RL, afterglow at 10 K, and temperature-dependent TL of (b) BA_2PbBr_4, (c) BA_2CuBr_4, and (d) BA_2SnBr_4 crystals. Afterglow parts were recorded after 10 minutes of X-ray irradiation at 10 K with heating rate of 0.14 K s^{-1} indicated by red-dashed lines.

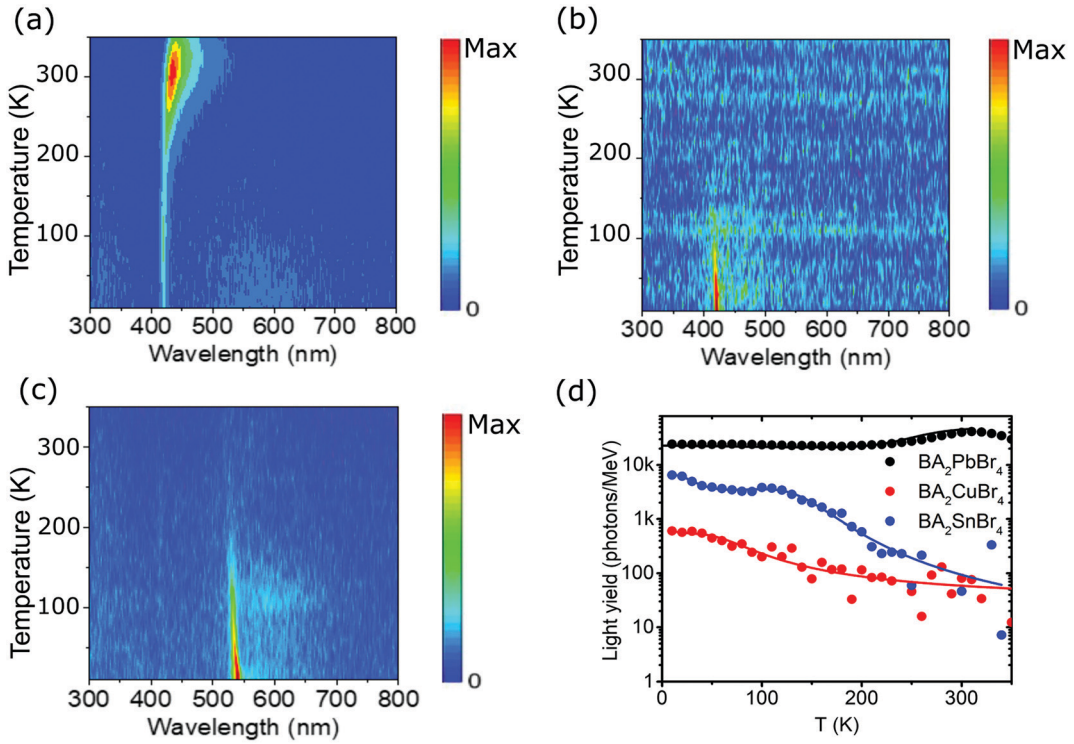

Fig. 4 RL spectra mapping at different temperatures from 10 to 350 K for (a) BA_2PbBr_4, (b) BA_2CuBr_4, and (c) BA_2SnBr_4 crystals. (d) Temperature-dependent light yield from 10 K to 350 K under 45 keV X-ray excitation. The full lines are the negative thermal quenching fits and the parameters are shown in Table S1 (ESI†).

The largest PLQY is reported for BA_2PbBr_4 at 36% and this value is still below the 79% of another 2D lead bromide perovskite crystal, BZA_2PbBr_4.[46] After including the PLQY for BA_2PbBr_4 and temperature-dependent light yield in Fig. 4(d), the new expected light yields become 41 000 and 73 000 photons per MeV for temperatures at 150 K and RT, respectively. Since the measured light yield at RT is 40 000 photons per MeV,[8] the transfer efficiency is therefore 55%. Unlike BA_2PbBr_4, both lead-free crystals show strong thermal quenching at RT, while at 150 K, Pb substitution with Cu or Sn leads to much lower measured light yields of 100 and 2000 photons per MeV, respectively.

Conclusion

In this work, we reported the effect of Pb replacement by Cu or Sn on the optical and scintillation properties previously reported for solution processed BA_2PbBr_4 perovskite crystal. Pb substitution with Cu or Sn leads to an E_g^{exp} red-shift from 3.59 to 3.90 and 3.44 eV, and a Stokes shift from 0.59 to 2.06 and 1.13 eV, respectively. The large Stokes shift should improve the light yield due to the potential reduction of self absorption.[7] Despite the large Stokes shift observed for BA_2CuBr_4 and BA_2SnBr_4, RL of these crystals at RT was hardly found. However, at 10 K, BA_2CuBr_4 and BA_2SnBr_4 did show narrow RL spectra with FWHM of 0.04 eV and 0.03 eV, respectively. For BA_2PbBr_4, the RL spectrum at 10 K with a FWHM of 0.05 eV is narrower than that at RT with a FWHM of 0.16 eV. Furthermore, temperature-dependent RL confirmed the negative thermal quenching in BA_2PbBr_4 crystal. On the other hand, we also observe strong thermal quenching for both lead-free crystals at RT, while at 150 K, BA_2CuBr_4 and BA_2SnBr_4 exhibited low measured light yields of 100 and 2000 photons per MeV, respectively. Beside low light yield, Pb replacement by Cu or Sn also induced slower PL decay times from 3.0 ns to 1.3 and 8.5 μs, respectively. Although the cation replacement caused lowering of the scintillation performance, these findings may give insight into the design of lead-free perovskite scintillators.

Author contributions

Sample preparation, L. J. D., D. O., and I. M.; optical characterization, PLQY, XRD, and X-ray imaging, F. M., D. K., and M. D. B.; XPS and Raman characterization, A.; DFT calculations, M. H. M.; RL and TL characterization, A. B., M. E. W., M. M., and W. D.; data analysis and writing, D. K., M. D. B., L. J. D., and L. J.; supervision, W. D. and M. D. B. All authors have read and agreed to the published version of the manuscript.

Conflicts of interest

There are no conflicts to declare.

Acknowledgements

This work is part of the project that has received funding from the Indonesian Ministry of Research, Technology and Higher

Education through INSINAS RISET PRATAMA scheme (No. 47/INS-1/PPK/E4/2018 and 35/INS-1/PPK/E4/2019), WCR No. 079/E4.1/AK.04.PT/2021, Institut Teknologi Bandung under the 'Riset ITB 2022' scheme (No. 223/IT1.B07.1/TA.01/2022), and Ministry of Education, Singapore (Award No. MOE2018-T2-1-088). RL and TL measurements were performed at the National Laboratory for Quantum Technologies (NLTK), Nicolaus Copernicus University and supported by the European Regional Development Fund. Mimin Aminah is acknowledged for her technical support in the sample preparation.

Notes and references

1 F. Maddalena, L. Tjahjana, A. Xie, Arramel, S. Zeng, H. Wang, P. Coquet, W. Drozdowski, C. Dujardin, C. Dang and M. D. Birowosuto, *Crystals*, 2019, **9**, 88.
2 Q. Chen, J. Wu, X. Ou, B. Huang, J. Almutlaq, A. A. Zhumekenov, X. Guan, S. Han, L. Liang, Z. Yi, J. Li, X. Xie, Y. Wang, Y. Li, D. Fan, D. B.-L. Teh, A. H. All, O. F. Mohammed, O. M. Bakr, T. Wu, M. Bettinelli, H. Yang, W. Huang and X. Liu, *Nature*, 2018, **561**, 88–93.
3 N. Kawano, M. Koshimizu, G. Okada, Y. Fujimoto, N. Kawaguchi, T. Yanagida and K. Asai, *Sci. Rep.*, 2017, **7**, 14754.
4 M. D. Birowosuto, D. Cortecchia, W. Drozdowski, K. Brylew, W. Lachmanski, A. Bruno and C. Soci, *Sci. Rep.*, 2016, **6**, 37254.
5 J. H. Heo, D. H. Shin, J. K. Park, D. H. Kim, S. J. Lee and S. H. Im, *Adv. Mater.*, 2018, **30**, 1801743.
6 Y. Zhang, R. Sun, X. Ou, K. Fu, Q. Chen, Y. Ding, L.-J. Xu, L. Liu, Y. Han, A. V. Malko, X. Liu, H. Yang, O. M. Bakr, H. Liu and O. F. Mohammed, *ACS Nano*, 2019, **13**, 2520–2525.
7 R. T. Williams, W. W. Wolszczak, X. Yan and D. L. Carroll, *ACS Nano*, 2020, **14**, 5161–5169.
8 A. Xie, F. Maddalena, M. E. Witkowski, M. Makowski, B. Mahler, W. Drozdowski, S. V. Springham, P. Coquet, C. Dujardin, M. D. Birowosuto and C. Dang, *Chem. Mater.*, 2020, **32**, 8530–8539.
9 A. Xie, C. Hettiarachchi, F. Maddalena, M. E. Witkowski, M. Makowski, W. Drozdowski, Arramel, A. T.-S. Wee, S. V. Springham, P. Q. Vuong, H. J. Kim, C. Dujardin, P. Coquet, M. D. Birowosuto and C. Dang, *Commun. Mater.*, 2020, **1**, 37.
10 Y. Li, L. Chen, B. Liu, P. Jin, R. Gao, L. Zhou, P. Wan, Q. Xu and X. Ouyang, *J. Mater. Chem. C*, 2021, **9**, 17124–17128.
11 F. Maddalena, A. Xie, Arramel, M. E. Witkowski, M. Makowski, B. Mahler, W. Drozdowski, T. Mariyappan, S. V. Springham, P. Coquet, C. Dujardin, M. D. Birowosuto and C. Dang, *J. Mater. Chem. C*, 2021, **9**, 2504–2512.
12 H. Hardhienata, F. Ahmad, Arramel, M. Aminah, D. Onggo, L. J. Diguna, M. D. Birowosuto, M. E. Witkowski, M. Makowski and W. Drozdowski, *J. Phys. D: Appl.Phys.*, 2020, **53**, 455303.
13 A. Arramel, A. D. Fauzi, X. Yin, C. S. Tang, M. H. Mahyuddin, M. Sahdan, M. Aminah, D. Onggo, G. Shukri, C. Diao, H. Wang, M. D. Birowosuto, A. Wee and A. Rusydi, *Commun. Mater.*, 2021, **2**, 70.
14 L. J. Diguna, S. Kaffah, M. H. Mahyuddin, Arramel, F. Maddalena, S. A. Bakar, M. Aminah, D. Onggo, M. E. Witkowski, M. Makowski, W. Drozdowski and M. D. Birowosuto, *RSC Adv.*, 2021, **11**, 20635–20640.
15 Q. He, C. Zhou, L. Xu, S. Lee, X. Lin, J. Neu, M. Worku, M. Chaaban and B. Ma, *ACS Mater. Lett.*, 2020, **2**, 633–638.
16 J. Cao, Z. Guo, S. Zhu, Y. Fu, H. Zhang, Q. Wang and Z. Gu, *ACS Appl. Mater. Interfaces*, 2020, **12**, 19797–19804.
17 J. Rodríguez-Carvajal, *Phys. B*, 1993, **192**, 55–69.
18 Arramel, F. Maddalena, M. H. Mahyuddin, X. Yin, C. S. Tang, M. K. Agusta, M. F. Sahdan, C. Diao, C. Dang, M. D. Birowosuto, A. T.-S. Wee and A. Rusydi, *Mater. Today Energy*, 2022, **24**, 100921.
19 P. Hohenberg and W. Kohn, *Phys. Rev.*, 1964, **136**, B864–B871.
20 W. Kohn and L. J. Sham, *Phys. Rev.*, 1965, **140**, A1133–A1138.
21 G. Kresse and J. Furthmüller, *Comput. Mater. Sci.*, 1996, **6**, 15–50.
22 G. Kresse and J. Furthmüller, *Phys. Rev. B*, 1996, **54**, 11169–11186.
23 P. E. Blöchl, *Phys. Rev. B*, 1994, **50**, 17953–17979.
24 G. Kresse and D. Joubert, *Phys. Rev. B*, 1999, **59**, 1758–1775.
25 J. P. Perdew, K. Burke and M. Ernzerhof, *Phys. Rev. Lett.*, 1996, **77**, 3865–3868.
26 S. L. Dudarev, G. A. Botton, S. Y. Savrasov, C. J. Humphreys and A. P. Sutton, *Phys. Rev. B*, 1998, **57**, 1505–1509.
27 L. Wang, T. Maxisch and G. Ceder, *Phys. Rev. B*, 2006, **73**, 195107.
28 H. J. Monkhorst and J. D. Pack, *Phys. Rev. B: Solid State*, 1976, **13**, 5188–5192.
29 S. Grimme, J. Antony, S. Ehrlich and H. Krieg, *J. Chem. Phys.*, 2010, **132**, 154104.
30 K. Persson, *Materials Data on CuBr2 (SG:12) by Materials Project*, 2016.
31 A. Varghese, Y. Yin, M. Wang, S. Lodha and N. Medhekar, *arXiv*, 2021, preprint, arXiv:2108.07488.
32 K. X. Steirer, P. Schulz, G. Teeter, V. Stevanovic, M. Yang, K. Zhu and J. J. Berry, *ACS Energy Lett.*, 2016, **1**, 360–366.
33 Z. Ahmad, M. A. Najeeb, R. A. Shakoor, A. Alashraf, S. A. Al-Muhtaseb, A. Soliman and M. K. Nazeeruddin, *Sci. Rep.*, 2017, **7**, 15406.
34 Arramel, A. Xie, X. Yin, C. S. Tang, M. H. Mahyuddin, C. Hettiarachchi, M. F. Sahdan, K. Yoshizawa, C. Dang, M. D. Birowosuto, A. T.-S. Wee and A. Rusydi, *ACS Appl. Energy Mater.*, 2020, **3**, 7500–7511.
35 Arramel, A. Xie, X. Yin, C. S. Tang, A. D. Fauzi, X. Chi, C. Diao, M. F. Sahdan, M. D. Birowosuto, C. Dang, A. Rusydi and A. T.-S. Wee, *ACS Appl. Mater. Interfaces*, 2020, **12**, 4114–4122.
36 L.-J. Xu, H. Lin, S. Lee, C. Zhou, M. Worku, M. Chaaban, Q. He, A. Plaviak, X. Lin, B. Chen, M.-H. Du and B. Ma, *Chem. Mater.*, 2020, **32**, 4692–4698.
37 T. Sheikh, A. Shinde, S. Mahamuni and A. Nag, *ACS Energy Lett.*, 2018, **3**, 2940–2946.

38 T. Sheikh, A. Shinde, S. Mahamuni and A. Nag, *Mater. Res. Express*, 2019, **6**, 124002.
39 C. Zhou, W. Chen, S. Yang, Q. Ou, Z. Gan, Q. Bao, B. Jia and X. Wen, *ACS Appl. Mater. Interfaces*, 2020, **12**, 26384–26390.
40 H. Guthrey and J. Moseley, *Adv. Energy Mater.*, 2020, **10**, 1903840.
41 B. Febriansyah, T. Borzda, D. Cortecchia, S. Neutzner, G. Folpini, T. M. Koh, Y. Li, N. Mathews, A. Petrozza and J. England, *Angew. Chem., Int. Ed.*, 2020, **59**, 10791–10796.
42 L. Lanzetta, J. M. Marin-Beloqui, I. Sanchez-Molina, D. Ding and S. A. Haque, *ACS Energy Lett.*, 2017, **2**, 1662–1668.
43 H. Shibata, *Jpn. J. Appl. Phys.*, 1998, **37**, 550–553.
44 M. Nikl, *Meas. Sci. Technol.*, 2006, **17**, R37.
45 J. C. de Mello, H. F. Wittmann and R. H. Friend, *Adv. Mater.*, 1997, **9**, 230–232.
46 X. Gong, O. Voznyy, A. Jain, W. Liu, R. Sabatini, Z. Piontkowski, G. Walters, G. Bappi, S. Nokhrin, O. Bushuyev, M. Yuan, R. Comin, D. McCamant, S. O. Kelley and E. H. Sargent, *Nat. Mater.*, 2018, **17**, 550–556.